Electronic Supplementary Information

Formation of cobalt-oxygen intermediates by dioxygen activation at a mononuclear nonheme cobalt(II) center

Deesha D. Malik,[a] Anirban Chandra,[b] Mi Sook Seo,[a] Yong-Min Lee,[a] Erik R. Farquhar,[c] Stefan Mebs,[d] Holger Dau,[d] Kallol Ray,*[,b] and Wonwoo Nam*[,a]

[a] *Department of Chemistry and Nano Science, Ewha Womans University, Seoul 03760, Korea*

[b] *Department of Chemistry, Humboldt-Universität zu Berlin, Brook-Taylor-Straße 2, 12489 Berlin, Germany*

[c] *Case Center for Synchrotron Biosciences, NSLS-II, Brookhaven National Laboratory Upton, NY 11973, USA*

[d] *Freie Universität Berlin, FB Physik, Arnimallee 14, 14195 Berlin, Germany*

*To whom correspondence should be addressed.

E-mail: wwnam@ewha.ac.kr; kallol.ray@chemie.hu-berlin.de

Table of Contents

Table S1. Crystallographic data and refinements for **1**-BPh_4.

	1-BPh_4
Empirical formula	C45 H68 Co N10 B
Formula weight	758.74
Temperature (K)	296.15
Wavelength (Å)	0.71073
Crystal system/space group	Monoclinic, *P2(1)/n*
Unit cell dimensions	
a (Å)	17.8648(18)
b (Å)	19.110(2)
c (Å)	18.2001(19)
α (°)	90
β (°)	91.7957(13)
γ (°)	90
Volume (Å^3)	6210.2(11)
Z	6
Calculated density (g/cm^{-3})	1.2172
Absorption coefficient (mm^{-1})	0.326
F(100)	2438.1511
Reflections collected	11020
Absorption correction	multi-scan (T_{min} = 0.7073, T_{max}= 0.7452)
Independent reflections [*R*(int)]	9194
Data/restraints/parameters	11020/0/750
Goodness-of-fit on F^2	1.0451
Final R indices [$F^2 > 2\sigma(F^2)$]	R_1 = 0.0307, wR_2 = 0.0702
R indices (all data)	R_1 = 0.0416, wR_2 = 0.0755
Largest difference peak and hole (e/Å^3)	0.252 and –0.345

Table S2. Selected bond distances (Å) and angles (º) for **1**-BPh_4.

Bond Distances (Å)	
Co1-N1	1.9850(13)
Co1-N5	1.9787(13)
Co1-N8	1.9921(13)
Co1-N4	2.0735(12)
Bond Angles (°)	
N5-Co1-N1	122.55(5)
N8-Co1-N1	117.66(5)
N8-Co1-N5	118.21(5)
N4-Co1-N1	84.84(5)
N4-Co1-N5	85.97(5)
N4-Co1-N8	86.68(5)

Table S3. Product analysis for the O_2-activation reactions by **1** with cyclohexene-h_{10} and cyclohexene-d_{10} in O_2-saturated acetone at 25 °C.

substrate	product	yield, %
cyclohexene-h_{10}	cyclohex-2-enol	16
	cyclohex-2-enone	20
	cyclohexene oxide	2
cyclohexene-d_{10}	cyclohex-2-enol	17
	cyclohex-2-enone	2
	cyclohexene oxide	19

Table S4. Results of the EXAFS simulations (fit)[a] for **2a**.

fit	Co-N/O			Co-O/N			Co•••C			ΔE_0	χ^2	R
	n	r	σ^2	n	r	σ^2	n	r	σ^2			
1	4	2.04	6.9							-0.78	14.09	0.0173
2	*5*	*2.03*	*8.9*							*-1.35*	*7.81*	*0.0096*
3	6	2.03	10.9							-1.88	15.72	0.0193
4	4	2.04	6.6	1	1.89	11.4				-2.94	15.94	0.0048
5	3	2.06	5.6	1	1.94	5.3				-0.91	34.56	0.0105
6	5	2.03	7.5	1	1.83	11.1				-4.32	10.78	0.0033
7	5	2.04	8.9							-1.49	48.78	0.1967
8	5	2.04	9.0				4	2.97	6.8	-0.46	39.01	0.1301
9	5	2.04	9.0				6	2.97	10.0	-0.50	42.58	0.1420
10	5	2.03	9.1				8	2.97	13.6	-0.71	48.63	0.1622
11	***5***	***2.04***	***9.0***				***4*** ***4***	***2.97*** ***3.40***	***6.7*** ***2.8***	***-0.80***	***9.65***	***0.0255***

[a] Fitting range was k = 2.0-12.4 Å^{-1} (resolution = 0.145 Å) with back transform ranges of 1-1.9 Å for fits 1-6 and 1-3.25 Å for fits 7-11. r is in units of Å; σ^2 is in units of 10^{-3} Å; ΔE_0 is in units of eV; R represents the fractional mis-fit of the data, while χ^2 is the χ^2 fitting metric normalized by the number of independent data points in a given fit.

Table S5. Results of the EXAFS simulations (fit) for **3** (Rf = 9.9%).

shell	N*	R	err	S*	err
Co-O	1	1.85	0.04	0.075	0.008
Co-N	4	2.03	0.02	0.075	
Co-C	4	2.86	0.03	0.075	
Co-C	3	3.06	0.05	0.075	
Co-C	8	3.40	0.02	0.075	

Table S6. Selected bond distances in DFT-optimized structures of $[(TMG_3tren)Co^{IV}(O)]^{2+}$, $[(TMG_3tren)Co^{IV}(O)(Sc(OTf)_3)]^{2+}$ and $[(TMG_3tren)Co^{IV}(O)\text{-}(Sc(OTf)(OH)_2)_2]^{2+}$ in the S = 3/2 state.

model	Co-N3	Co-N4	Co-N5	Co-N6	Co-O	O-Sc1	O-Sc2	Co-Sc1	Co-Sc2
$[(TMG_3tren)Co^{IV}(O)]^{2+}$	2.071	1.978	1.967	2.018	1.636	-	-	-	-
$[(TMG_3tren)Co^{IV}(O)(Sc(OTf)_3)]^{2+}$	2.075	1.970	1.964	1.972	1.739	1.880	-	3.619	-
$[(TMG_3tren)Co^{IV}(O)(Sc(OTf)(OH)_2)_2]^{2+}$	2.111	1.953	1.930	2.597	1.843	2.059	2.094	3.476	3.651

Table S7. Hammett parameters (σ_p^+) of *p*-X-substituted benzaldehydes and second-order rate constants (k_2) for the oxidation of *p*-X-substituted benzaldehydes by **2a** in acetone at 25 °C.

substrate	$\sigma_p^{+\,a}$	k_2, $M^{-1}\ s^{-1}$	log k_2
p-Me-PhCHO	-0.311	$3.0(3) \times 10^{-1}$	–0.52
p-F-PhCHO	-0.073	$6.8(5) \times 10^{-1}$	–0.17
PhCHO	0	$7.4(5) \times 10^{-1}$	–0.13
p-CN-PhCHO	0.659	4.1(4)	0.61

[a] Taken from the reference: Brown H. C.; Okamoto, Y. Electrophilic Substituent Constants. *J. Am. Chem. Soc.*, **1958**, 80, 4979- 4987.

Table S8. Second-order rate constants for the hydrogen atom transfer and oxygen atom transfer reactions by **2a** at 25 °C and **3** at 0 °C in acetone.

substrate	BDE,[a] kcal mol^{-1}	k_2, M^{-1} s^{-1}	
		2a	**3**
xanthene-h_2	75.5	$3.9(3) \times 10^{-1}$	$7.0(6) \times 10^{-1}$
xanthene-d_2	-	$8.4(6) \times 10^{-2}$	$3.1(3) \times 10^{-1}$
DHA	77	$1.0(1) \times 10^{-1}$	$2.9(2) \times 10^{-1}$
CHD	78	$6.8(5) \times 10^{-2}$	$7.5(6) \times 10^{-2}$
PPh_3	-	$8.4(5) \times 10^{-2}$	7.3(5)

[a] Taken from the reference 47 in Text.

Table S9. Product analysis for the hydrogen atom transfer and oxygen atom transfer reactions by **2a** at 25 °C and **3** at 0 °C in acetone.

substrate	product	yield, %	
		2a	**3**
xanthene	xanthone	40(3)	100(4)
DHA	anthracene	100(4)	60(4)
CHD	benzene	88(4)	40(3)
PPh_3	$Ph_3P{=}O$	100(4)	80(4)

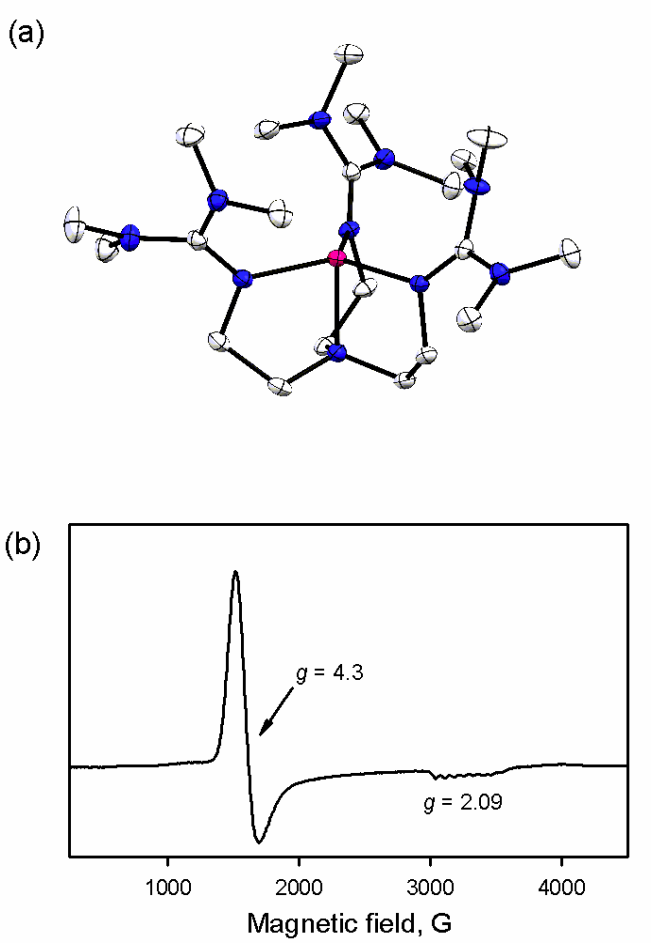

Fig. S1 (a) X-ray single crystal structure of $[(TMG_3tren)Co^{II}]^{2+}$ moiety in $[(TMG_3tren)Co^{II}](BPh_4)_2$ (**1**-BPh_4). Tetraphenyl borate anions and hydrogen atoms are omitted for clarity [Co, pink; N, blue; C, white] (see Tables S1 and S2 for the crystallographic data). (b) X-band CW-EPR spectrum of 1-BPh_4 in acetone at 5 K.

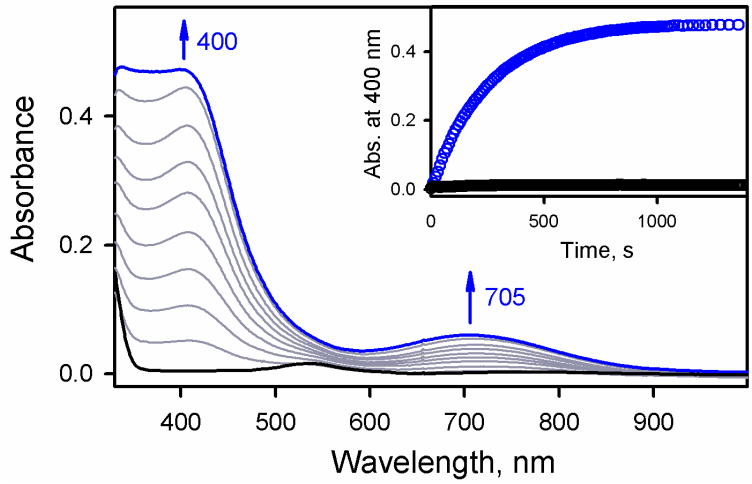

Fig. S2 UV-vis spectral changes for the formation of **2a** (blue line) in the O_2-activation reaction by **1** with THF upon addition of THF (0.20 M) to an O_2-saturated acetone solution of **1** (0.25 mM; black line) at 25 °C. Inset shows time courses monitored at 400 nm under O_2 (blue circle) and Ar (black circle) atmospheres in acetone at 25 °C.

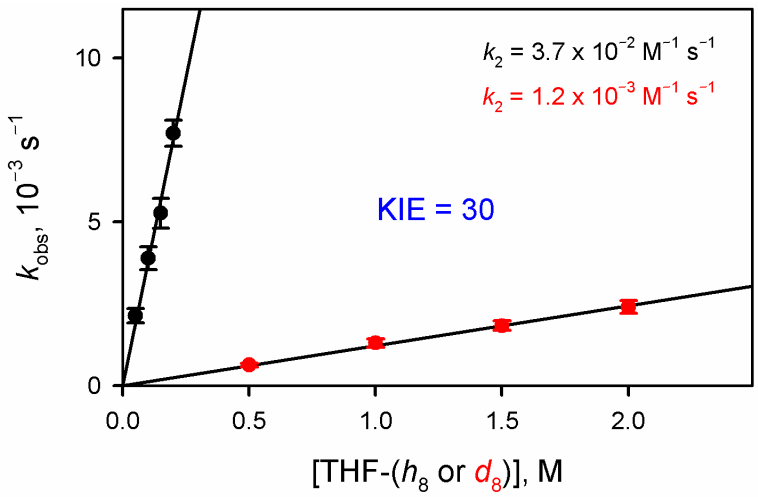

Fig. S3 Plots of pseudo-first-order rate constants (k_{obs}) against the concentration of THF (black circles) and THF-d_8 (red circles) for the formation of **2a** in the O_2-activation reaction by **1** in acetone at 25 °C to determine the second order rate constants (k_2) and KIE value.

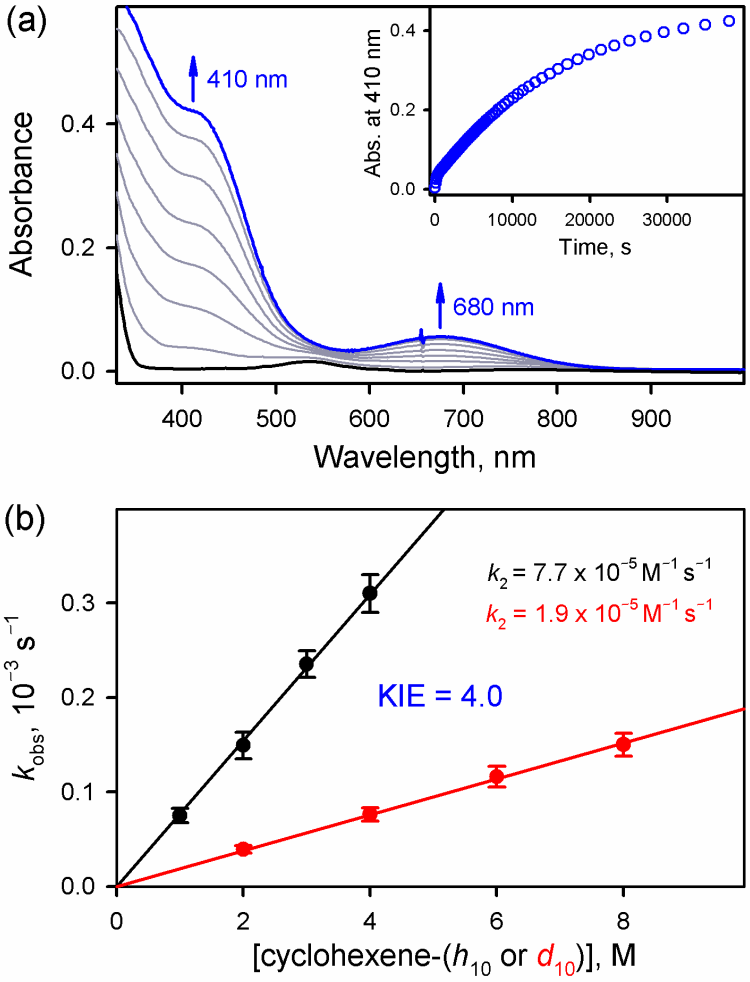

Fig. S4 (a) UV−vis spectral changes for the formation of **2b** (blue line) in the O_2-activation reaction by **1** upon addition of cyclohexene (1.0 M) to an O_2-saturated acetone solution of **1** (0.25 mM; black line) at 25 °C. Inset shows time course monitored at 410 nm due to **2b**. (b) Plots of pseudo-first-order rate constants (k_{obs}) against the concentration of cyclohexene (black circles) and cyclohexene-d_{10} (red circles) for the formation of **2b** in the O_2-activation reaction by **1** with cyclohexene-(h_{10} or d_{10}) in acetone at 25 °C to determine the second order rate constants (k_2) and KIE value.

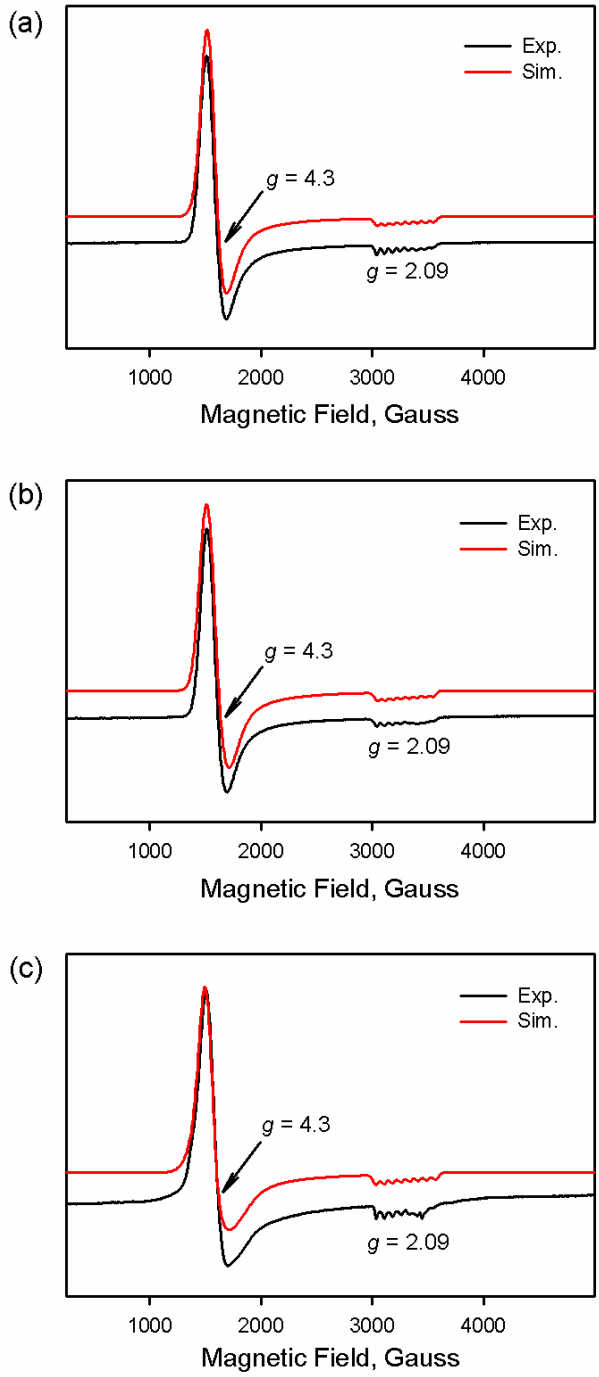

Fig. S5 X-band CW-EPR spectra (black lines) of (a) **2a** (1.0 mM), (b) **2b** (1.0 mM), and (c) **2c** (1.0 mM). Spectra were recorded in acetone at 5 K. Red lines show the simulated spectra. Simulation parameters: g = [2.09, 4.35, 4.45] and A = [213, 154, 84] G for **2a**, g = [2.09, 4.28, 4.51] and A = [210, 148, 84] G for **2b**, and g = [2.09, 4.29, 4.51] and A = [213, 154, 84] G for **2c**.

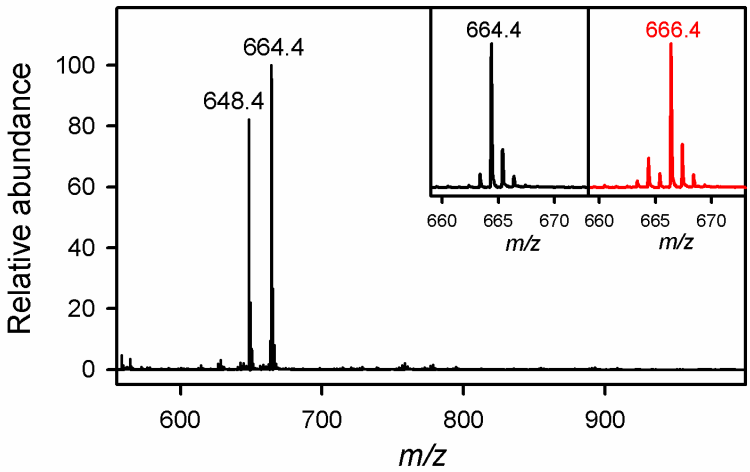

Fig. S6 Positive mode CSI-MS spectrum of **2b** produced in the O_2-activation reaction by **1** upon addition of cyclohexene (0.20 M) into an O_2-saturated acetone solution of **1** (0.25 mM) at 25 °C. The peaks at *m/z* = 664.4 and 648.4 correspond to $[Co^{IV}(O)(TMG_3tren)(OTf)]^+$ (calculated *m/z* = 664.3) and $[Co^{II}(TMG_3tren)(OTf)]^+$ (calculated *m/z* = 648.3), respectively. The insets show the observed isotope distribution patterns for $[Co^{IV}(^{16}O)(TMG_3tren)(OTf)]^+$ (*m/z* = 664.4) originated from **2b**-^{16}O (left panel) and $[Co^{IV}(^{18}O)(TMG_3tren)(OTf)]^+$ (*m/z* = 666.4) originated from **2b**-^{18}O (right panel).

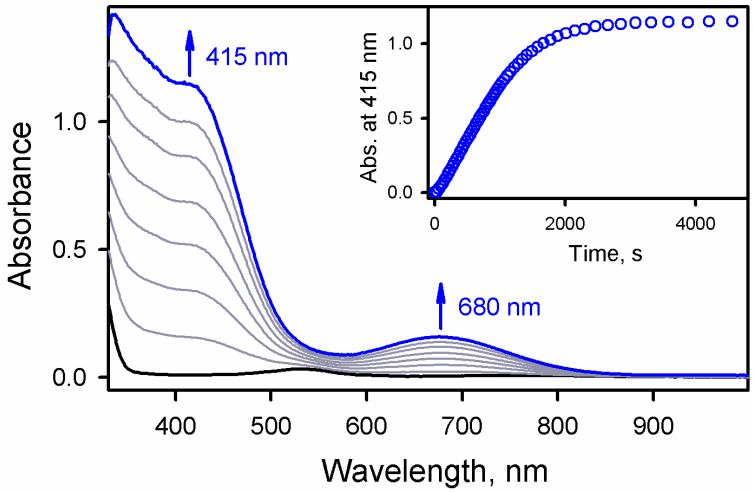

Fig. S7 UV−vis spectral changes for the formation of **2c** (blue line) observed in the reaction of **1** (0.25 mM; black line) and cumene hydroperoxide (CumOOH; 50 mM) in acetone at 25 °C. Inset shows time course monitored at 415 nm due to **2c**.

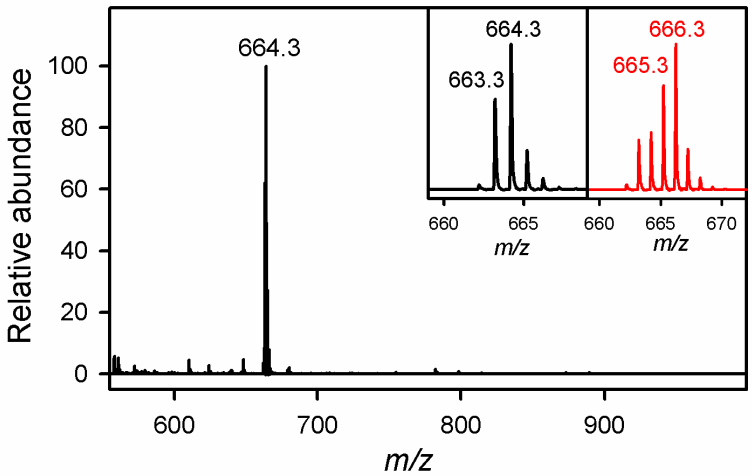

Fig. S8 Positive mode CSI-MS spectrum of **2c** produced in the reaction of **1** (0.25 mM) and cumene hydroperoxide (CumOOH; 50 mM) in acetone at 25 °C. The peaks at *m/z* = 663.3 and 664.3 correspond to $[Co^{III}(TMG_3tren\text{-}O)(OTf)]^+$ (calculated *m/z* = 663.3) and $[Co^{IV}(O)(TMG_3tren)(OTf)]^+$ (calculated *m/z* = 664.3), respectively. The insets show the observed isotope distribution patterns for $[Co^{III}(TMG_3tren\text{-}^{16}O)(OTf)]^+$ (*m/z* = 663.3) and $[Co^{IV}(^{16}O)(TMG_3tren)(OTf)]^+$ (*m/z* = 664.3) originated from **2c**-^{16}O (left panel) and $[Co^{III}(TMG_3tren\text{-}^{18}O)(OTf)]^+$ (*m/z* = 665.3) and $[Co^{IV}(^{18}O)(TMG_3tren)(OTf)]^+$ (*m/z* = 666.4) originated from **2c**-^{18}O (right panel), indicating that, when Cum^{18}O^{18}OH was used instead of Cum^{16}O^{16}OH, two mass unit shift from *m/z* = 663.3 and 664.3 to *m/z* = 665.3 and 666.3, respectively, was observed.

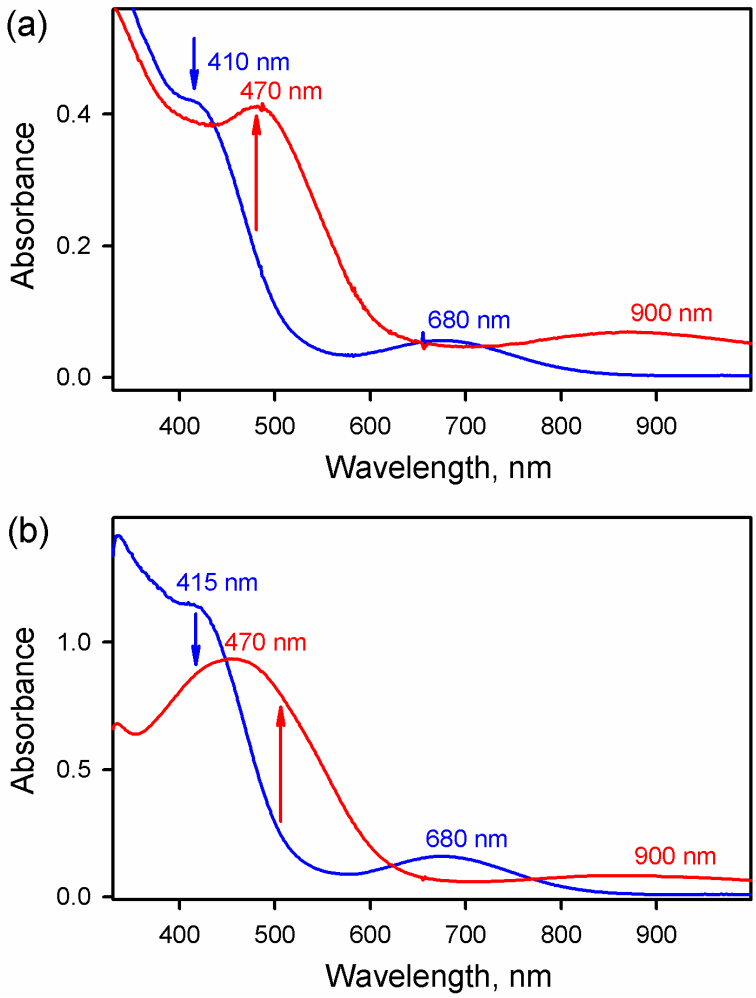

Fig. S9 UV−vis spectral changes for the formation of **3** (red line) from (a) **2b** (0.25 mM; blue line) and (b) **2c** (0.25 mM; blue line) upon addition of $Sc(OTf)_3$ (1.25 mM; 5.0 equiv.) to an acetone solution of **2b** and **2c** at –40 °C.

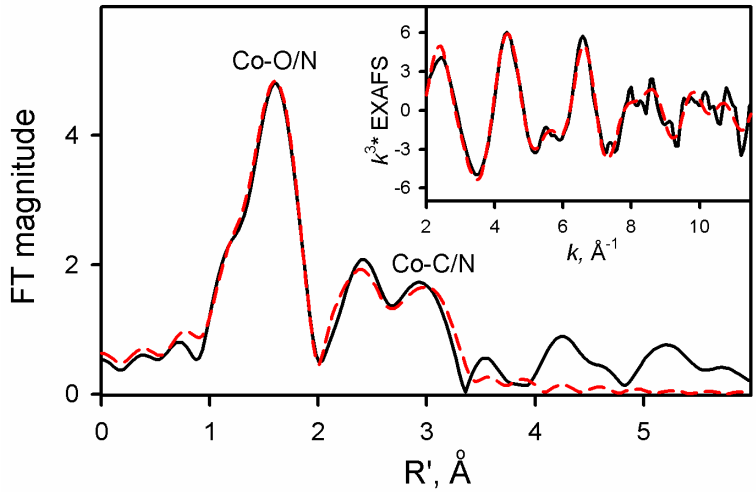

Fig. S10 Observed (black solid line) and simulated (red dashed line) Fourier-transformed EXAFS spectra of **3**. The inset shows the observed (black solid line) and simulated (red dashed line) EXAFS data on a wave-vector scale before calculation of the Fourier transform.

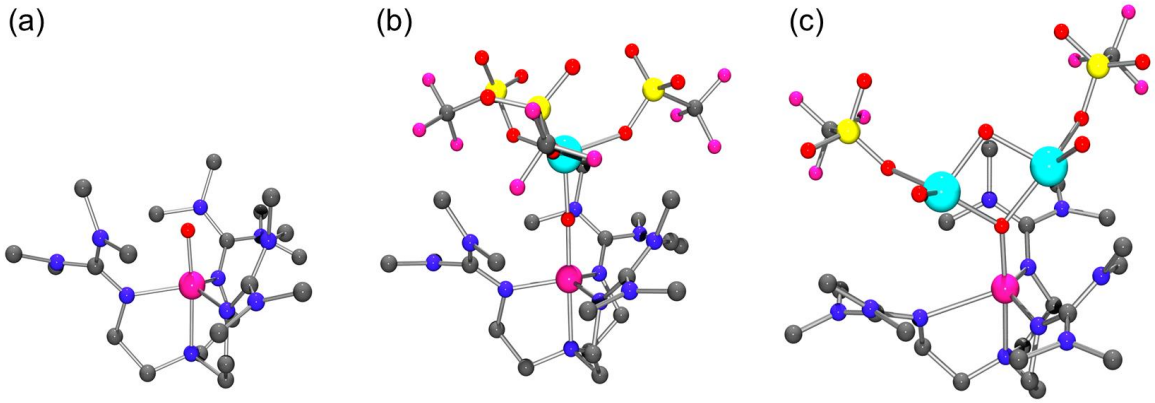

Fig. S11 DFT-optimized structures of (a) $[(TMG_3tren)Co^{IV}(O)]^{2+}$, (b) $[(TMG_3tren)Co^{IV}(O)(Sc(OTf)_3)]^{2+}$, and (c) $[(TMG_3tren)Co^{IV}(O)(Sc(OTf)(OH)_2)_2]^{2+}$.

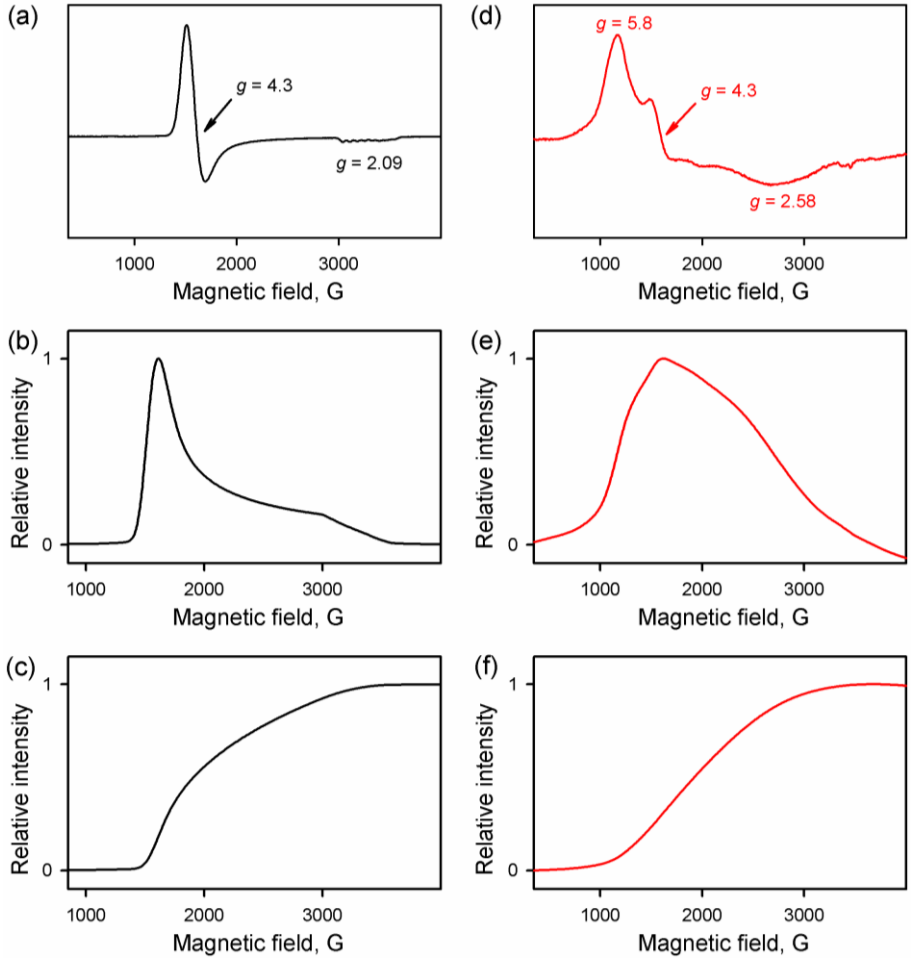

Fig. S12 First derivative (a, d), integrated (b, e) and doubly integrated (c, f) EPR spectra of (a, b, c) **1** and (d, e, f) **3** recorded in acetone at 5 K. **3** was generated by reacting **1** (1.0 mM) with THF (0.10 M) in the presence of $Sc(OTf)_3$ (2.0 mM) in O_2-saturated acetone at 0 ºC. The yield of the intermediate **3** was estimated to be 94%, which was calculated from the amount of **1** remained in the solution.

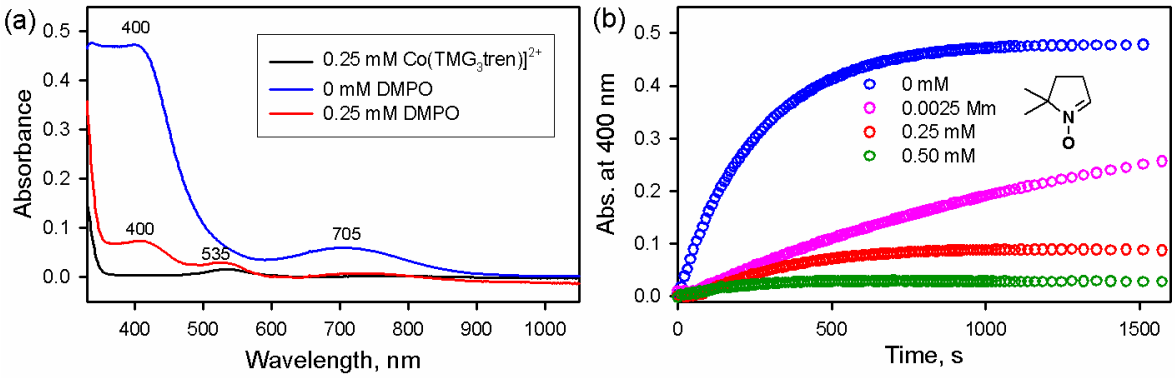

Fig. S13 UV−vis spectral changes observed upon addition of THF (0.20 M) to **1** (0.25 mM; black line) in the absence (blue line) and presence of DMPO (0.25 mM; red line) in O_2 saturated acetone at 25 ^{o}C. (b) Time profiles monitored for the change of absorbance at 400 nm due to **2a** for the O_2-activation by **1** (0.25 mM) with THF (0.20 M) in the absence and presence of DMPO (0 – 0.50 mM) in O_2 saturated acetone at 25 ^{o}C.

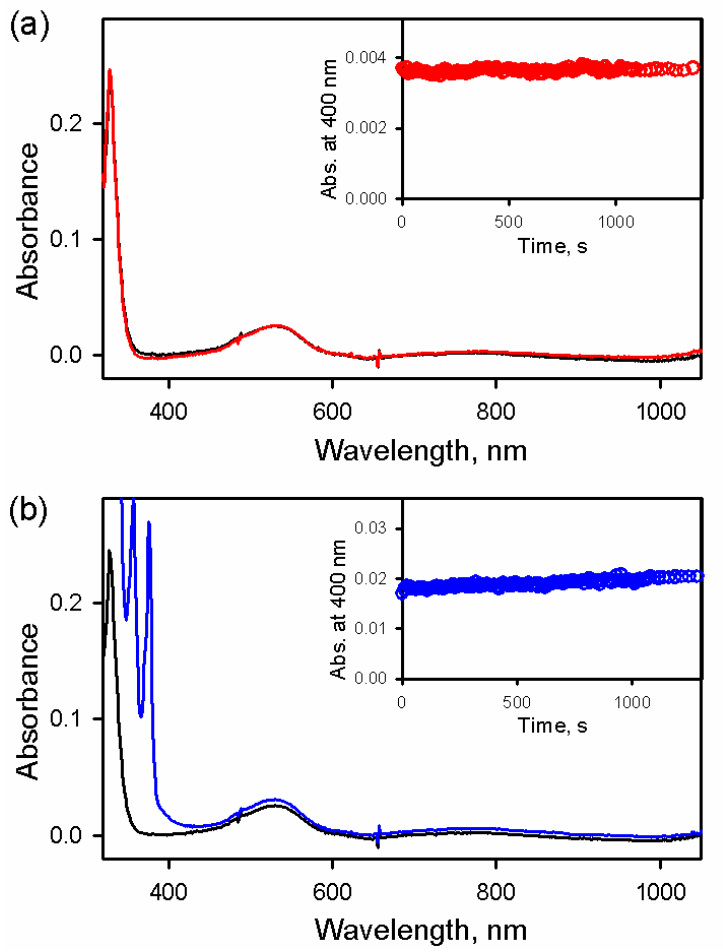

Fig. S14 UV−vis spectral changes upon addition of (a) 0.2 M 2,4 di-tert-butyl phenol (b) 0.2 M DHA to an acetone solution of **1** (0.25 mM; black line) at 25 °C.

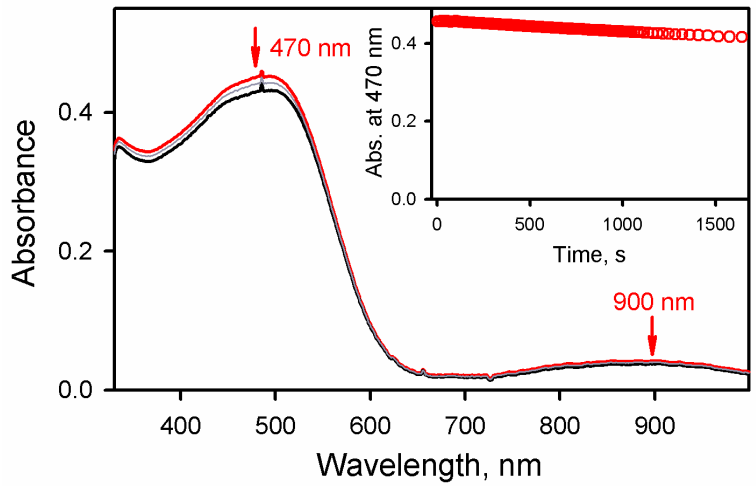

Fig. S15 UV-vis spectral changes observed in the reaction of **3** (0.25 mM) and CCA (50 mM) in acetone at 25 ºC. The rate is almost identical to that of natural decay of **3**.

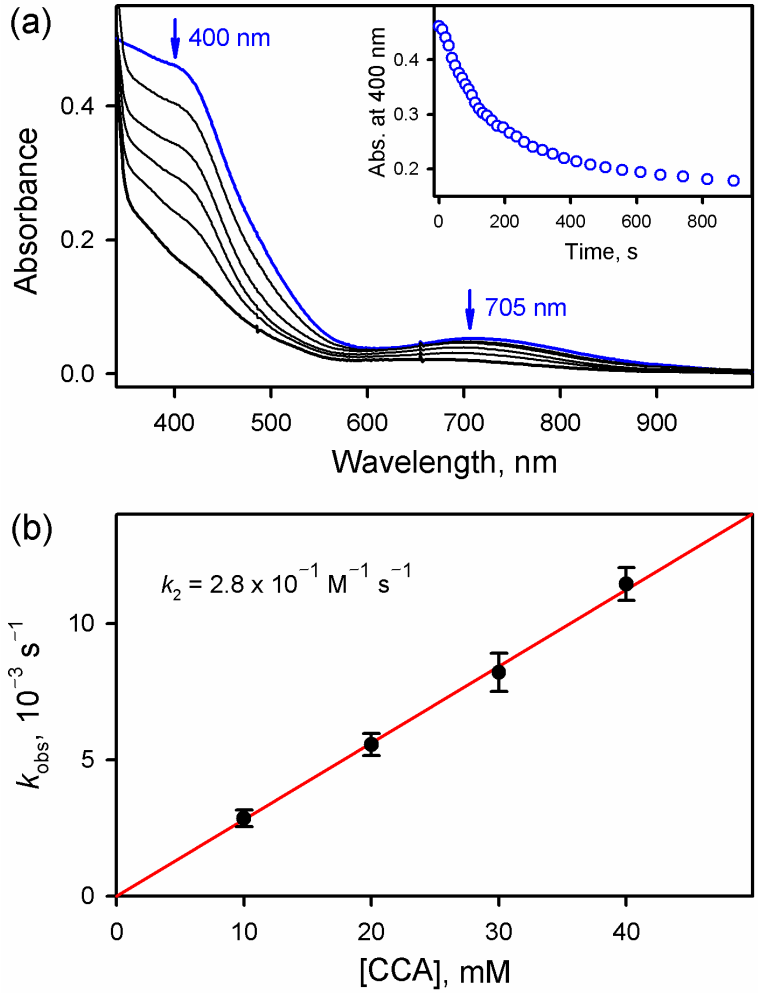

Fig. S16 (a) UV-vis spectral changes observed in the reaction of **2a** (0.25 mM) and CCA (20 mM) in acetone at 25 ºC. (b) Plot of pseudo-first-order rate constants (k_{obs}) against the concentration of CCA obtained in the deformylation reaction of CCA by **2a** in acetone at 25 °C to determine the second-order rate constants (k_2).

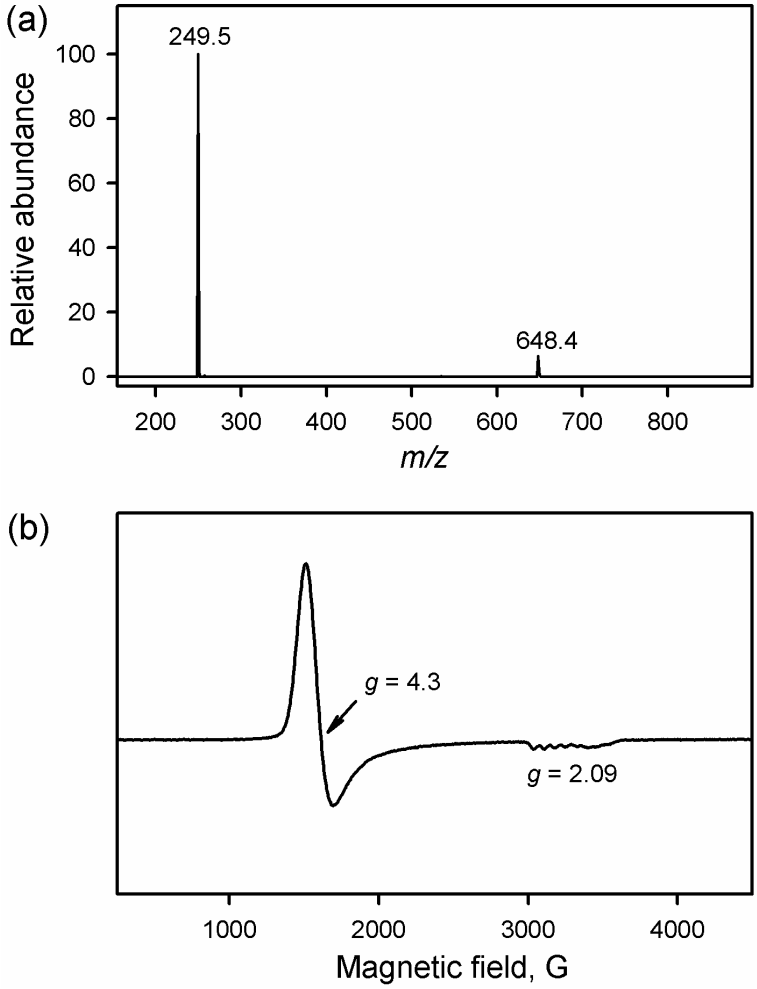

Fig. S17 (a) ESI-MS spectrum of the complete reaction solution obtained in the oxidation of CCA (20 mM) by **2a** (0.25 mM) in acetone at 25 ºC. The peaks at *m/z* = 249.5 and 648.4 correspond to $[Co^{II}(TMG_3tren)]^{2+}$ (calculated *m/z* = 249.5) and $[Co^{II}(TMG_3tren)(OTf)]^{+}$ (calculated *m/z* = 648.3), respectively. (b) X-band CW-EPR spectrum of the complete reaction solution obtained in the oxidation of CCA (20 mM) by **2a** (0.50 mM) in acetone at 25 ºC. Spectrum was recorded in acetone at 5 K.

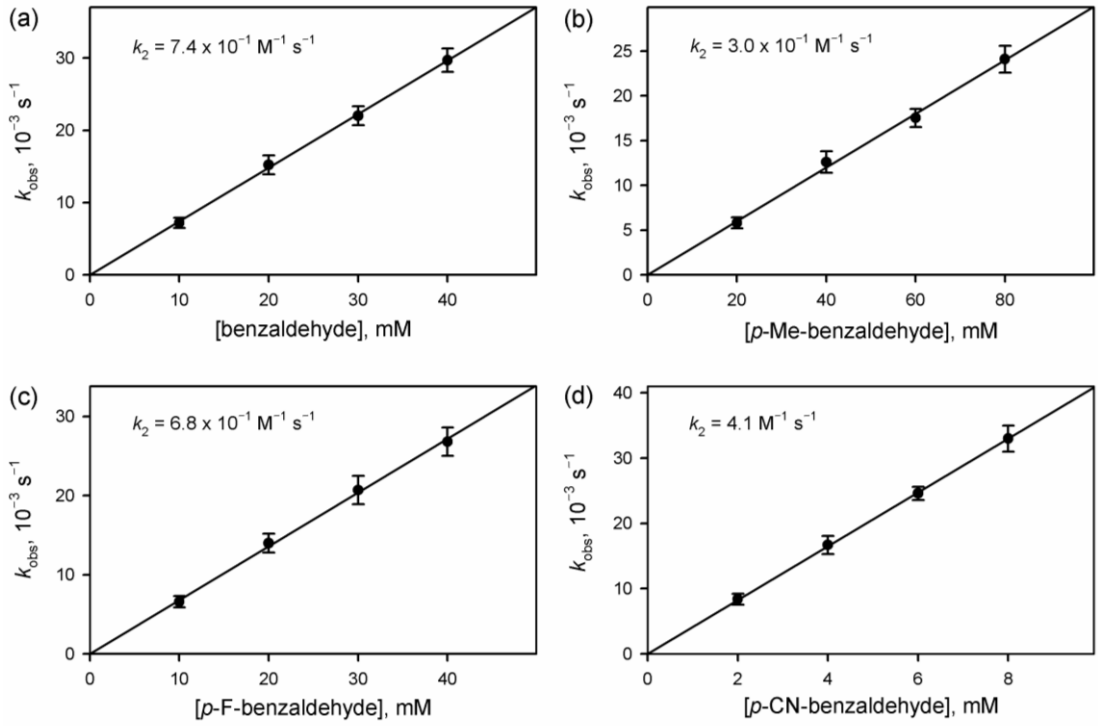

Fig. S18 Plots of pseudo-first-order rate constants (k_{obs}) against the concentration of *para*-X-benzaldehydes, (a) benzaldehyde, (b) *p*-methylbenzaldehyde, (c) *p*-fluorobenzaldehyde, and (d) *p*-cyanobenzaldehyde, obtained in the nucleophilic aldehyde deformylation reaction of *para*-X-benzaldehydes (X = Me, H, F, and CN) by **2a** in acetone at 25 °C to determine the second-order rate constants (k_2).

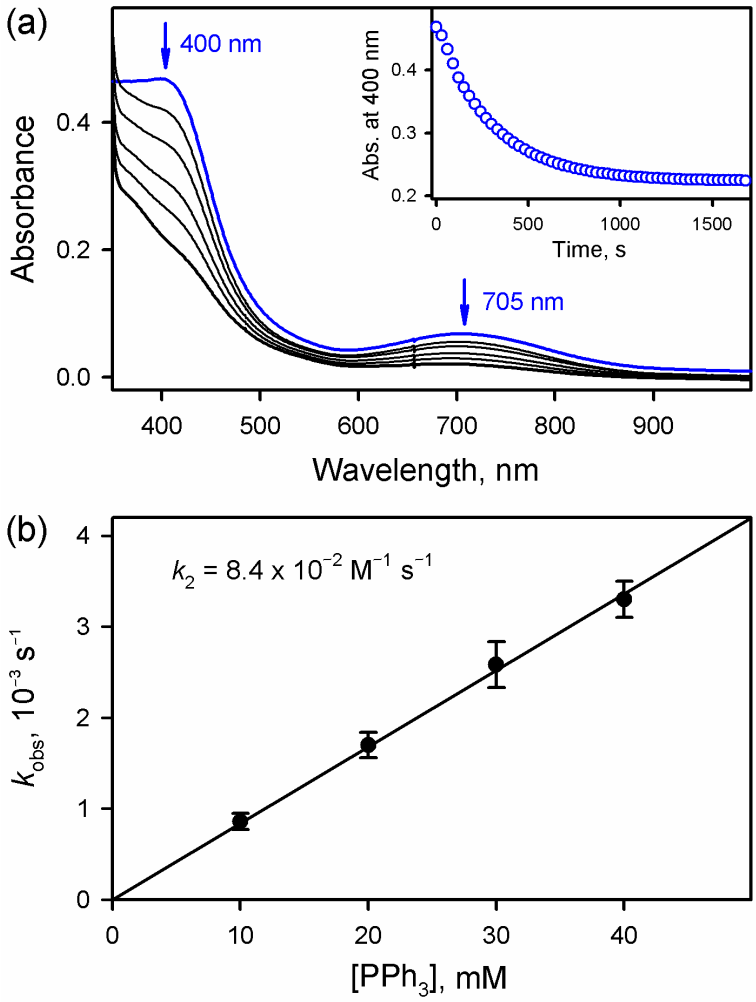

Fig. S19 (a) UV-vis spectral changes observed in the reaction of **2a** (0.25 mM) and triphenylphosphine (40 mM) in acetone at 25 °C. (b) Plots of pseudo-first-order rate constants (k_{obs}) against the concentration of triphenylphosphine to determine the second-order rate constant (k_2) for the reaction of **2a** with triphenylphosphine in acetone at 25 °C.

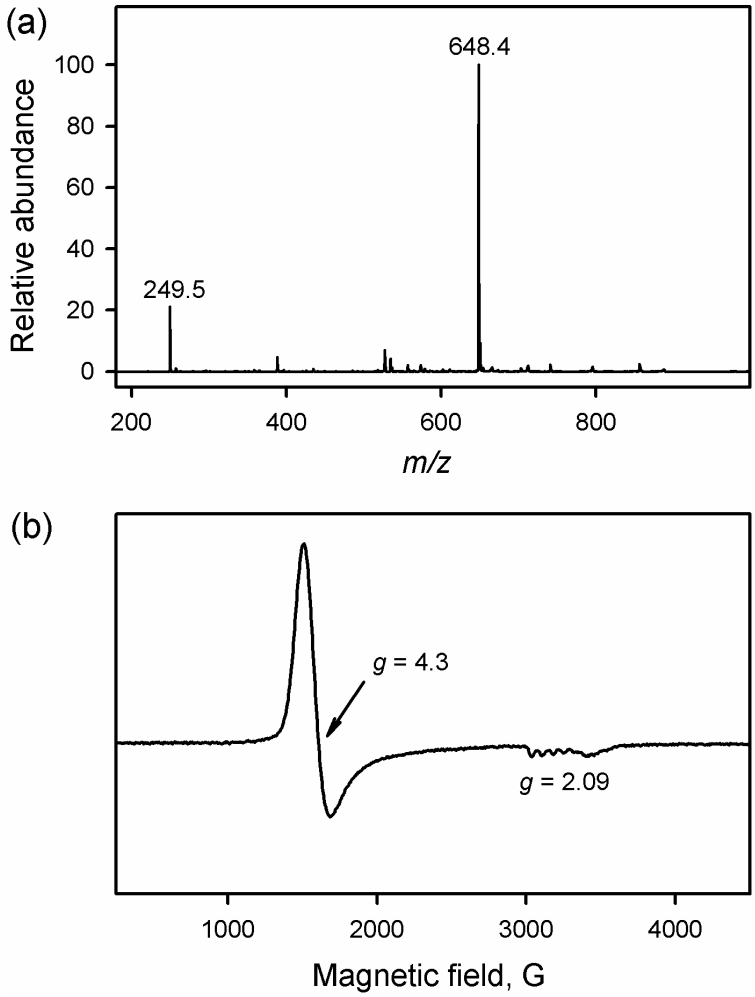

Fig. S20 (a) ESI-MS spectrum of the complete reaction solution obtained in the oxidation of PPh_3 (10 mM) by **2a** (0.25 mM) in acetone at 25 °C. The peaks at *m/z* = 249.5 and 648.4 correspond to $[Co^{II}(TMG_3tren)]^{2+}$ (calculated *m/z* = 249.5) and $[Co^{II}(TMG_3tren)(OTf)]^{+}$ (calculated *m/z* = 648.3), respectively. (b) X-band CW-EPR spectrum of the complete reaction solution obtained in the oxidation of PPh_3 (20 mM) by **2a** (0.50 mM) in acetone at 25 °C. Spectrum was recorded in acetone at 5 K.

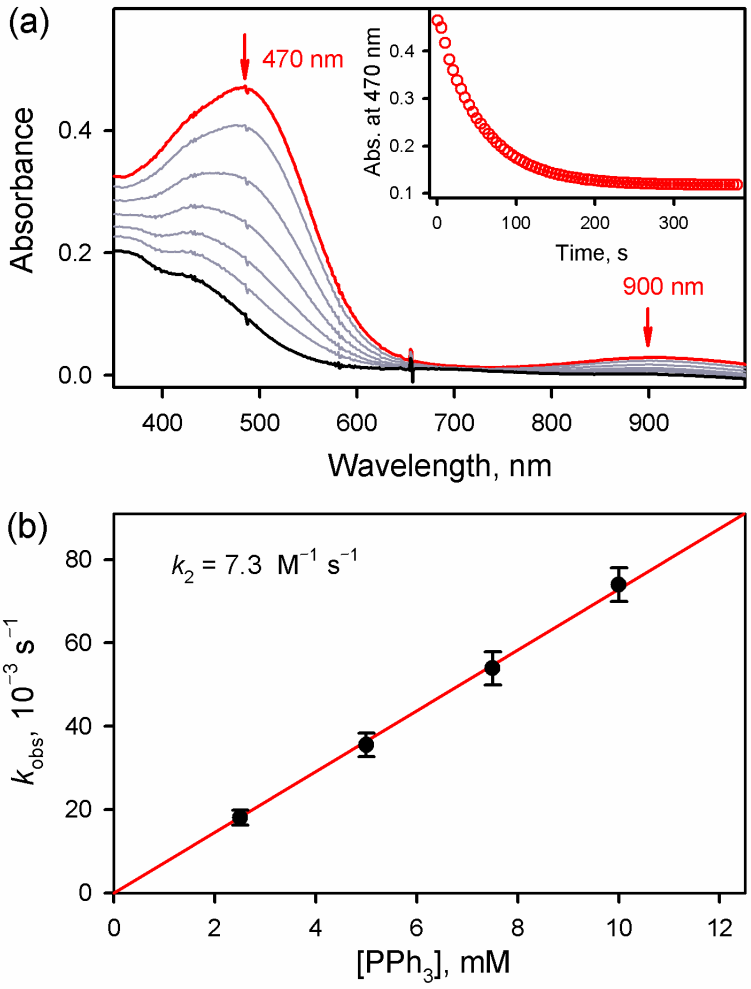

Fig. S21 (a) UV-vis spectral changes observed in the reaction of **3** (0.25 mM) with PPh_3 (2.5 mM) in acetone at 0 °C. (b) Plot of pseudo-first-order rate constants (k_{obs}) against the concentration of PPh_3 to determine the second-order rate constants (k_2) in the oxidation of PPh_3 by **3** in acetone at 0 °C.

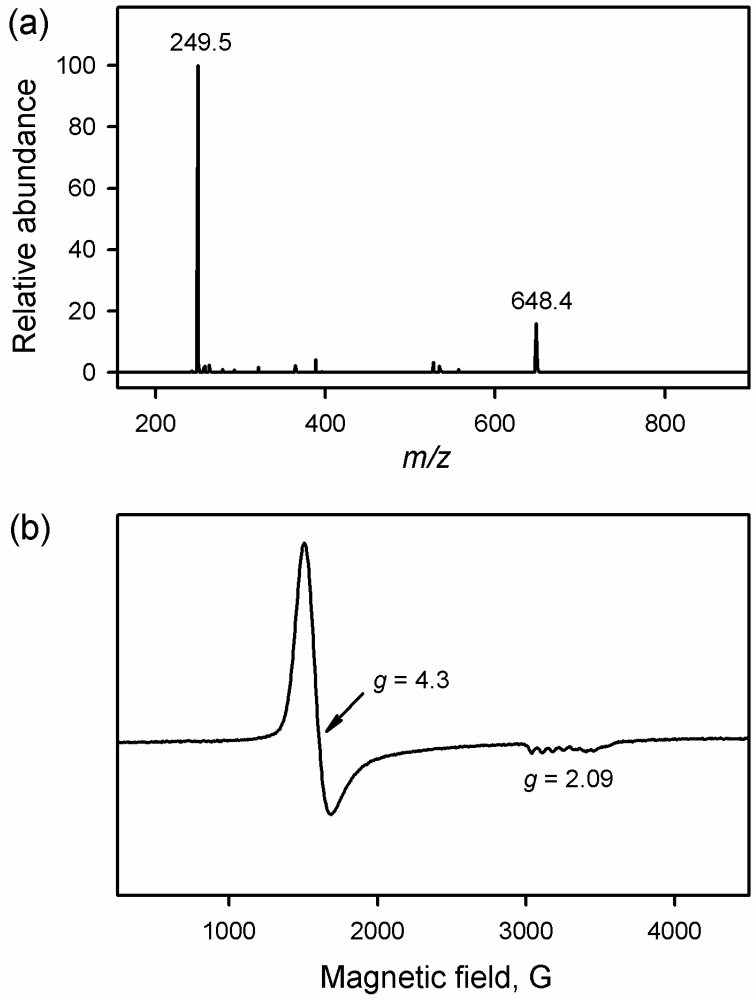

Fig. S22 (a) ESI-MS spectrum of the complete reaction solution obtained in the oxidation of PPh_3 (10 mM) by **3** (0.25 mM) in acetone at 0 ^{o}C. The peaks at *m/z* = 249.5 and 648.4 correspond to $[Co^{II}(TMG_3tren)]^{2+}$ (calculated *m/z* = 249.5) and $[Co^{II}(TMG_3tren)(OTf)]^{+}$ (calculated *m/z* = 648.3), respectively. (b) X-band CW-EPR spectrum of the complete reaction solution obtained in the oxidation of PPh_3 (10 mM) by **3** (0.50 mM) in acetone at 0 ^{o}C. Spectrum was recorded in acetone at 5 K.

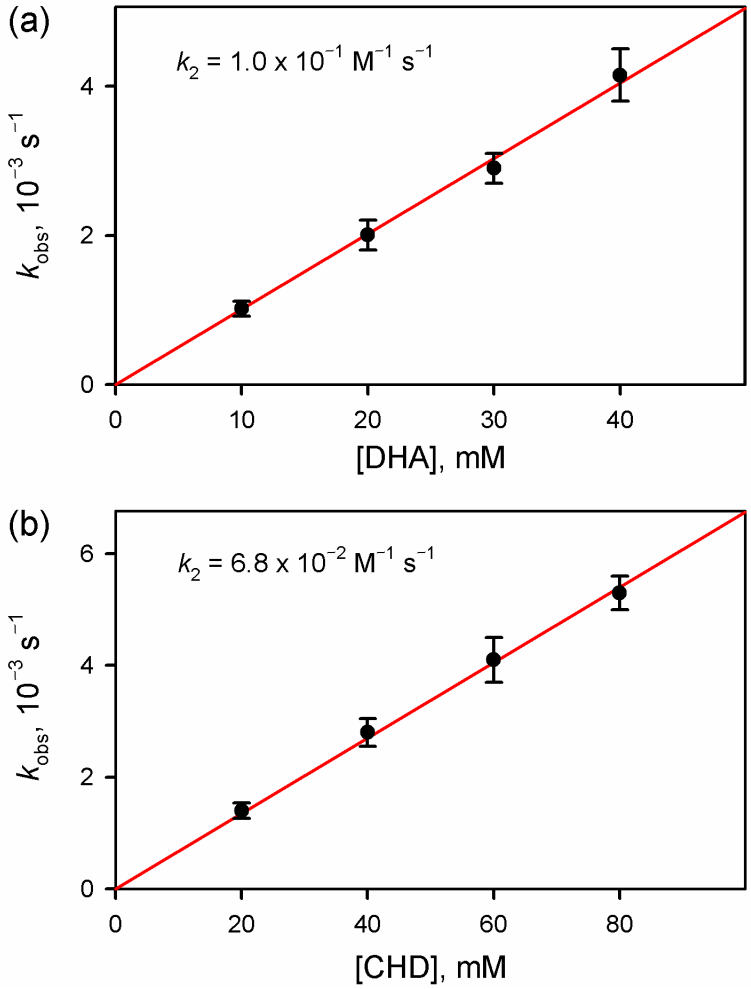

Fig. S23 Plots of pseudo-first-order rate constants (k_{obs}) against the concentration of substrates [(a) 9,10-dihydroanthracene (DHA) and (b) 1,4-cyclohexadiene (CHD)] to determine the second-order rate constants (k_2) in the C–H bond activation reaction of DHA and CHD by **2a** in acetone at 25 °C.

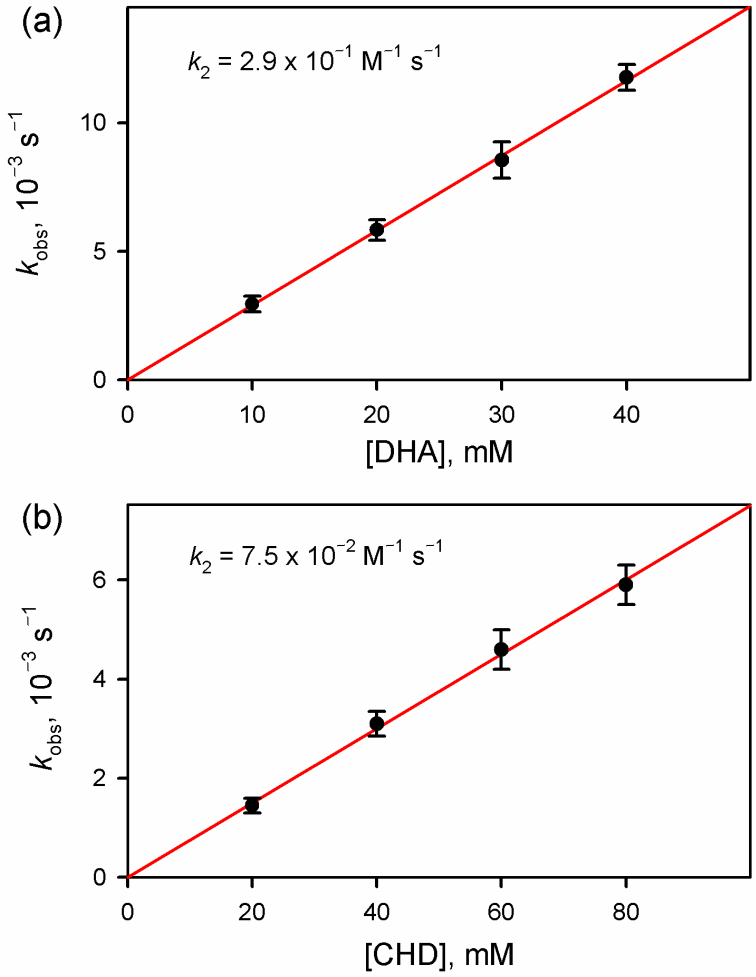

Fig. S24 Plots of pseudo-first-order rate constants (k_{obs}) against the concentration of substrates [(a) 9,10-dihydroanthracene (DHA) and (b) 1,4-cyclohexadiene (CHD)] to determine the second-order rate constants (k_2) in the C–H bond activation reaction of DHA and CHD by **3** in acetone at 0 °C.

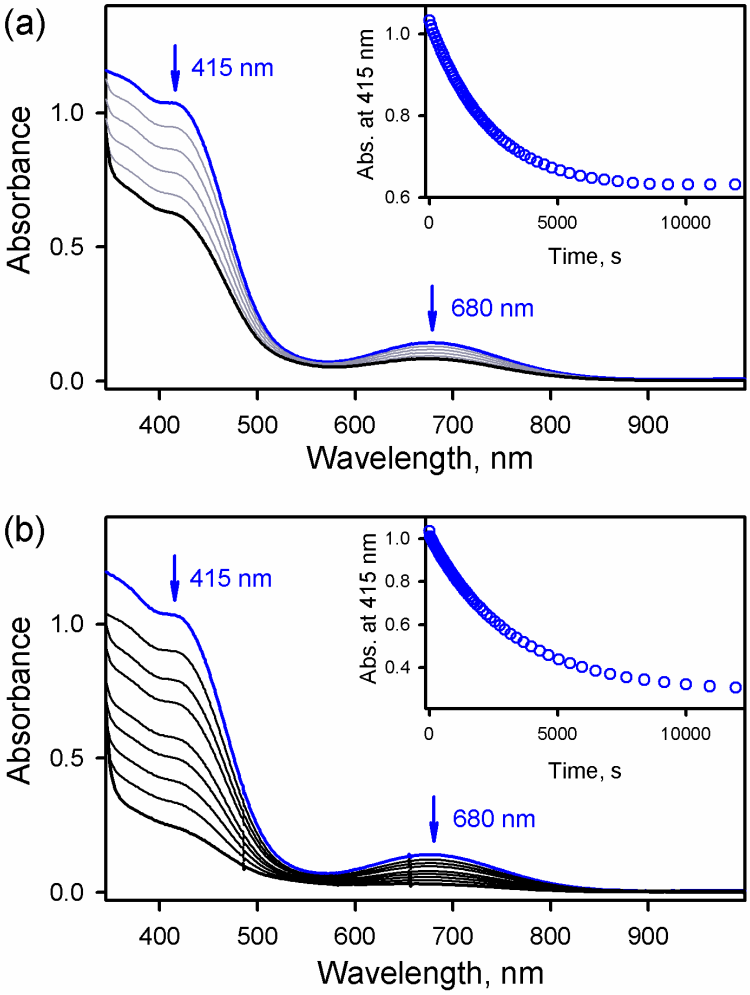

Fig. S25 UV-vis spectral changes observed in the oxidation of (a) xanthene (50 mM) and (b) triphenylphosphine (50 mM) by **2c** (0.25 mM) in acetone at 25 ^{o}C. The Insets show time courses monitored at 415 nm due to **2c**.

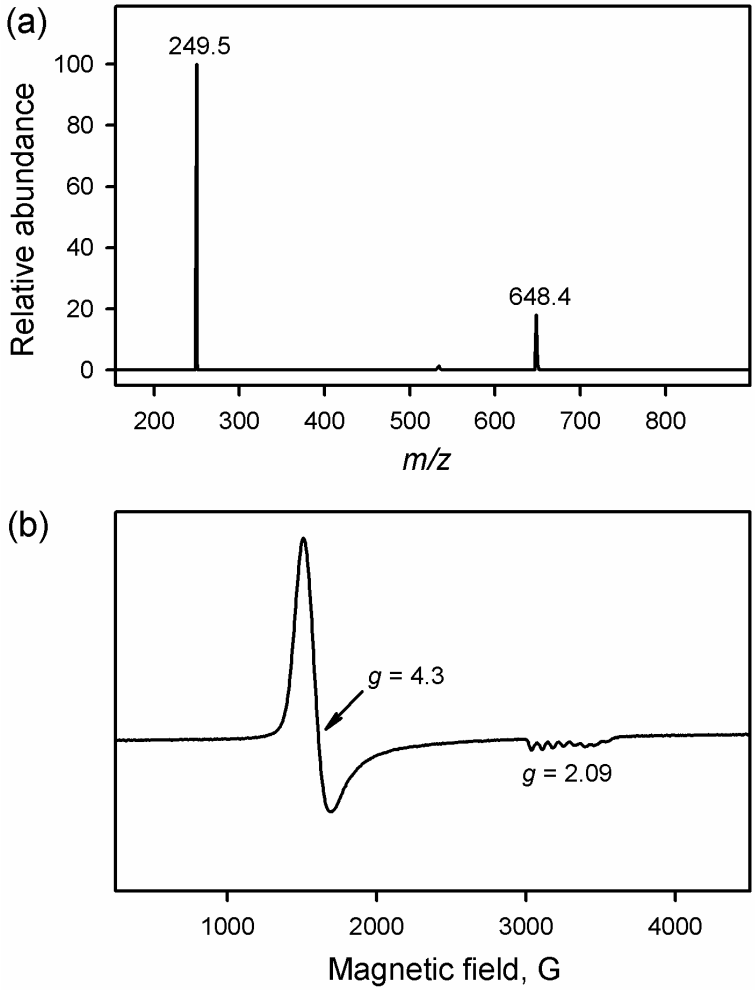

Fig. 26 (a) ESI-MS spectrum of the complete reaction solution obtained in the oxidation of xanthene (20 mM) by **2a** (0.25 mM) in acetone at 25 ^{o}C. The peaks at *m/z* = 249.5 and 648.4 correspond to $[Co^{II}(TMG_3tren)]^{2+}$ (calculated *m/z* = 249.5) and $[Co^{II}(TMG_3tren)(OTf)]^{+}$ (calculated *m/z* = 648.3), respectively. (b) X-band CW-EPR spectrum of the complete reaction solution obtained in the oxidation of xanthene (20 mM) by **2a** (0.50 mM) in acetone at 25 ^{o}C. Spectrum was recorded in acetone at 5 K.

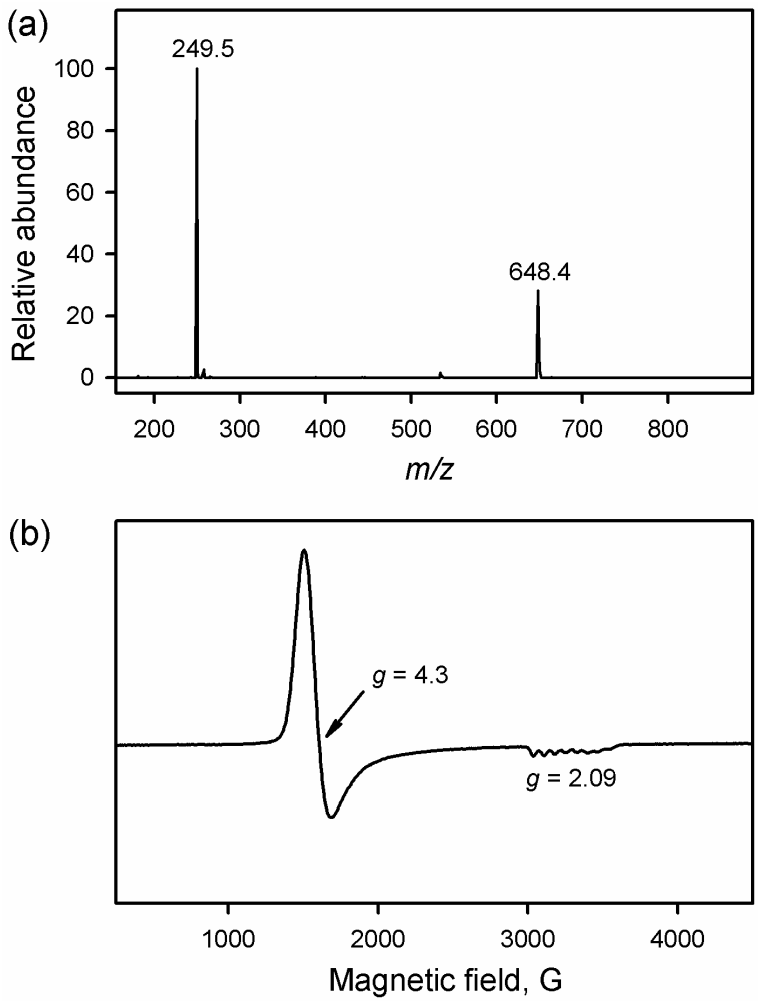

Fig. S27 (a) ESI-MS spectrum of the complete reaction solution obtained in the oxidation of xanthene (20 mM) by **3** (0.25 mM) in acetone at 0 °C. The peaks at *m/z* = 249.5 and 648.4 correspond to $[Co^{II}(TMG_3tren)]^{2+}$ (calculated *m/z* = 249.5) and $[Co^{II}(TMG_3tren)(OTf)]^{+}$ (calculated *m/z* = 648.3), respectively. (b) X-band CW-EPR spectrum of the complete reaction solution obtained in the oxidation of xanthene (20 mM) by **3** (0.25 mM) in acetone at 0 °C. Spectrum was recorded in acetone at 5 K.